An Integrated EMI Choke With Improved DM Inductance

Javad Borsalani, Ali Dastfan, and Javad Ghalibafan

***Abstract*—Utilizing electromagnetic interference (EMI) filters is a major approach to reduce the conducted emissions from the power electronic converters. These filters enlarge the total volume and weight of the system. Many works have been done to integrate the filter components. In this article a new integrated choke with a certain winding structure, consists of two core, a toroid, and a solenoid is presented. Although the DM inductance of the proposed choke could be independently increased by designing the windings, the CM inductance value remains almost constant as the conventional choke. Theoretical analysis for modeling the choke and prediction of the inductances and saturation conditions is provided. Experimental measurements validate the analysis, and show a good filtering performance with rejecting conducted noise from an induction motor drive system while it decreases the overall filter size.**

***Index Terms*—Choke, common mode (CM), differential mode (DM), DM inductance, electromagnetic interference (EMI), EMI filter, integrated choke.**

I. Introduction

REDUCTION of electromagnetic interference (EMI) is one of the major challenges in designing power electronic converters like switching power supplies and motor drive systems. The EMI emissions mainly come from high *dv/dt* and *di/dt* caused by the switch turn-ON and turn-OFF process [1]. The EMI noise should meet the relevant electromagnetic compatibility (EMC) standards such as CISPR and IEC, which restrict the conducted noise levels from 150 kHz up to 30 MHz [2], [3].

Utilizing the EMI filters is one of the basic approaches to reduce the noise level. These filters suppress both common-mode (CM) and differential-mode (DM) EMI noises. The CM noise represents the noise flowing between the power paths and the ground, while the DM noise usually flows within the power paths. The conventional passive EMI filter is usually contained *CL* configuration as the CM filter and inductor-capacitor *(LC)* or *CLC* configuration as the DM filter [4]. The CM capacitors are connected between the power line and the ground and their capacitances are restricted by the maximum allowed leakage current. Therefore, the CM inductance must be large enough, in order of milli-henries, to attain the required attenuation. The CM inductance is traditionally prepared by a CM choke, which should be able to carry the line current, causes to be heavy and big sized. The leakage inductance of a CM choke is usually determined as DM inductance but in most cases the leakage inductance is not enough large. However, two additional inductors are usually employed to improve the DM performance which more enlarges the filter size. Generally, there is no specific design limitation on the DM capacitance and is obtained based on the DM inductance. As the DM capacitor is connected between the power lines, its voltage should be equal or more than the nominal line voltage [5]. This leads the DM capacitor to be relatively large. As a result, the EMI filters are one of the largest functional units in the power electronic converters which usually account for up to 50% of the total volume and weight of the converter [5].

There has been a considerable amount of works to reduce the size and improve the performance of the EMI filter. The integration of the EMI filter components, usually the *LC* unit, can reduce the filter size. In [6], the design method and analysis model of an integrated EMI filter with flexible multilayer foils were presented, which properly reduced the total filter volume. Deng *et al.* [7] integrated both the EMI filter and boost inductor of a PFC converter on a mixed *EEE*-shape core using flexible multilayer foils, which reduces the total converter size. Chen *et al.* [8] proposed a structural winding capacitance cancellation method that utilized an embedded conductive ground layer in the planar inductor winding of an integrated filter. Using this method, both the equivalent parallel capacitance (EPC) of the inductor and the overall size of the filter have been reduced, but the CM performance at a high frequency has been influenced comparing to the discrete EMI filters. Wang and Xu [9] proposed an integrated annular *LC* unit and developed a generalized arc transmission theory to model it. The planar EMI filter structures were also proposed to integrate the filter components [10]. Based on the printed circuit board (PCB) process technology the structures were presented in [11], which reduce filter volume.

Some papers used active filtering methods to reduce filter volume. An active cancellation circuit has been proposed to reduce the low-frequency CM noise in a motor drive which was integrated on the inverter PCB [12]. Three winding CM inductors have been recently proposed, which boosted up the inductance leading to more attenuation at low-frequency noise and smaller size of the filter [13]. The integrated hybrid filter that consists of an active EMI filter with a passive one was proposed

Manuscript received July 18, 2019; revised October 19, 2019, January 7, 2020, February 26, 2020, and May 16, 2020; accepted July 3, 2020. Date of publication July 17, 2020; date of current version September 22, 2020. Recommended for publication by Associate Editor F. Costa. *(Corresponding author: Ali Dastfan.)*

The authors are with the Faculty of Electrical and Robotic Engineering, Shahrood University of Technology, Shahrood 3619995161, Iran (e-mail: j.borsalani@shahroodut.ac.ir; dastfan@shahroodut.ac.ir; jghalibafan@shahroodut.ac.ir).

Color versions of one or more of the figures in this article are available online at https://ieeexplore.ieee.org.

Digital Object Identifier 10.1109/TPEL.2020.3010131

in [14], which reduced to overall bulkiness. The combined magnetic integration of the harmonic and EMI filters is proposed recently for a single-phase grid-connected inverter using the EE-type magnetic core [15].

In some other works, the integrated EMI chokes have been proposed to improve the leakage inductance as DM inductance and minimize the size. Maillet *et al.* [16] increased the leakage inductance by placing the DM choke within the open window of the CM choke. In [17], a three-phase hybrid magnetic core was presented using two toroidal cores. The performance of these approaches was restricted in the high-frequency region. Tan *et al.* [18] presented a CM choke with a toroid-EQ mixed structure, which increased the DM inductance and decreased the parasitic coupling between the choke and the filter capacitors. Chu *et al.* [19] proposed a stacked CM inductor which consists of two CM inductors with identical cores, which improved the immunity of choke to the external magnetic fields and increased the DM inductance; however, the total volume of the choke has been increased. An integrated ac choke was proposed for a neutral-connected converter system that incorporated the CM suppression function into a DM inductor and reduced the volume and weight [20]. As a drawback, the DM inductance cannot be independently adjusted to the desired value in all of these previous works.

The integration of CM and DM inductors had been already addressed by using the core with the air-gapped intermediate magnetic branch [21]. Utilizing the EE-type core was reported for integration in some works which have the advantages of limited near-field emissions and total filter volume and weight reduction [15], [22]. In these structures, the same magnetic materials and air-gap length were used for CM and DM magnetic paths. Therefore, a large core size with more CM turns was used to have more CM inductance in the face of air-gap. On the other hand, the DM number of turns was restricted to prevent core saturation caused by high DM peak or dc currents. This fact hinders reducing the core volume of these works [23]. Umetani *et al.* [24] proposed a novel structure that assigned more turns to DM inductance. This structure suppressed dc saturation more effectively but the core not had a common shape and was hard to be manufactured. A certain integrated filter was presented in [25] for low-power ac drives with long cable leads. This integrated *RL* filter utilized JD-type cores to prepare DM flux paths and to match the CM and DM impedance to typical cable surge impedance.

This article presents a new integrated EMI choke based on the certain winding strategy. The choke consists of a conventional toroid core and a solenoid core, which is placed within the open area of the toroid. The main idea in the proposed choke is based on the use of a new winding strategy to adjust the DM inductance, while the CM inductance value remains almost constant. With the aid of this winding strategy, the CM magnetic flux path is prepared within the toroid core with high relative permeability material and without air-gap. As a result, further reduction in the core volume is expected to compare to the previous works with CM air-gapped core types [22] and [23]. Moreover, the DM magnetic flux path is consisting of four parts: the solenoid core, two small air-gaps between cores, and one half of the toroid core.

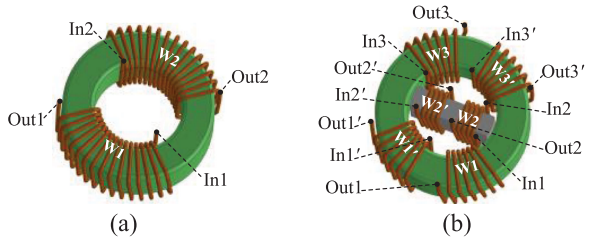

Fig. 1. 3-D view of the EMI choke. (a) Conventional choke. (b) Proposed choke.

As the magnetic material of the solenoid core can be selected with lower relative permeability than toroid, the DM saturation phenomenon of the proposed choke is effectively controlled. Another advantage of the proposed choke is that the DM inductance is significantly increased and can be independently controlled by the number of the solenoid windings turns and the CM inductance remains almost constant as conventional choke, which is not addressed in similar works. Finite element simulation results are presented to show the magnetic flux densities of the cores and then the designable parameters are developed to prevent the core saturation. The experimental measurements show that the proposed filter suppresses the noise up to 20 dB more than the conventional filter.

II. Winding Structures of the Proposed Choke

Fig. 1(a) shows an EMI choke used in the regular passive EMI filters [26], known as the conventional choke. The choke is based on a toroidal core with two equal and symmetric windings with *N*-turns. According to the right-hand law, the current directions of the windings are considered so that the induced fluxes become in the same direction, e.g., clockwise (CW) in Fig. 1(a). In conventional choke, the CM inductance is provided by the mutual inductance between winding 1 and 2, and the DM inductance is only achieved by the leakage fluxes of the windings, where the external DM inductor does not exist.

Our proposed EMI choke is shown in Fig. 1(b). It is made by two cores, one conventional toroidal core and one solenoid with a rectangular cross section, which is inserted in the internal air space of the toroid. To achieve better frequency performance, both cores are made of ferromagnetic material, e.g., ferrite and Mn-Zn. Six independent copper windings are mounted on the cores, four windings 1, 1′, 3, and 3′ on the toroid and two windings 2 and 2′ on the solenoid. To obtain the symmetrical shape, the windings 1, 1′, 3, and 3′ have an equal number of the turns with the same wire cross section, and also winding 2 and 2′ are homogeneous. For comparison between proposed and conventional choke, it is assumed that the windings 1, 1′, 3, and 3′ have N_T and windings 2 and 2′ have N_S number of turns. The N_T and N_S are the choke parameters and can be calculated in the EMI filter design steps based on the required CM and DM inductances, respectively. According to the right-hand law, the current direction of each winding is specified so that for CM current in the toroid core, the direction of the induced flux of all windings becomes CW, and in the solenoid core, the flux of two windings attenuates each other, as can be seen from

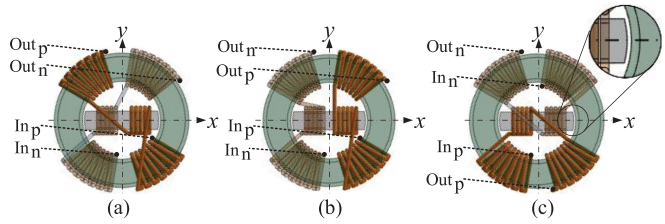

Fig. 2. Windings connections of the different choke structures. (a) Case A. (b) Case B. (c) Case C.

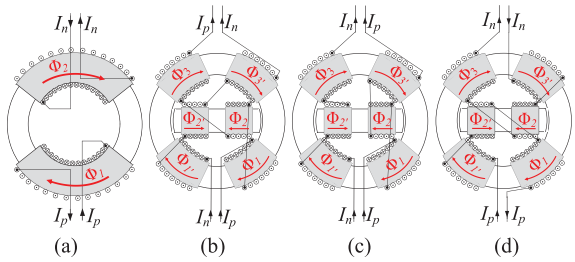

Fig. 3. Directions of the flux linking each winding of the choke refer to (a) conventional (b) case A (c) case B, and (d) case C.

Fig. 1(b). Each power path (phase and null) can be constructed by connecting three windings of the proposed EMI choke in series. To obtain the symmetrical paths, it can be shown that 24 different winding connections are possible; there exist four unique winding strategies. One of them has the best DM performance, which is considered as the proposed winding structure and another does not offer any appreciable benefits compared to conventional design. However, to justify the advantages of the proposed winding strategy and to shorten the discussions, only three cases with different winding strategies are presented and analyzed here, and the worth case is not considered. The winding connections are shown in Fig. 2 and introduced below. To attain a better view, the phase path is bolded.

Case A [see Fig. 2(a)]: The output phase current path of the winding 1 is connected to the input of winding 2 and the output of 2 to the input of 3. The null path is provided by connecting $1'$, $2'$, and $3'$ in series.

Case B [see Fig. 2(b)]: The output phase current path of the winding 1 is connected to the input of winding 2 and the output of 2 to the input of $3'$. The null path is provided by connecting $1'$, $2'$, and 3 in series. The choke is symmetrical relative to the *y*-axis.

Case C [see Fig. 2(c)]: The output phase current path of the winding $1'$ is connected to the input of winding $2'$ and the output of $2'$ to the input of 1. The null path is provided by connecting $3'$, 2, and 3 in series. The choke is symmetrical relative to the *x*-axis.

In all cases, the coupling between phase and null paths is properly made, which is desired for CM inductance. Furthermore, the windings on the solenoid core will improve the DM inductance. The air-gaps between cores are maintained constant by proper forming the end-section of the solenoid as can be seen in the zoomed area in Fig. 2(c).

It should be noted that, other winding strategies are possible in our proposed choke as an alternative of case C, i.e., connecting 1, $1'$, and $2'$ in series for the phase path or even not splitting the winding on the toroid. The analysis shows that these cases have almost similar performance to case C. However, case C is used for the modeling and theoretical analysis of this article based on the similarity of this case to cases A and B.

III. Theoretical Analysis of the Proposed Chokes

A. Choke Modeling

The noise current flows through the phase and null paths generate flux in the cores. Considering the conventional choke, the flux produced by each winding consists of two components: a leakage component denoted by *l* subscript and a magnetizing component denoted by m subscript. The leakage flux is the part that generated by current flowing in a winding, and it links only the turns of that winding. Likewise, the magnetizing flux is produced by a winding and it links all turns of both windings on the core. Therefore, the flux linking each winding on the conventional choke can be expressed as

$$\Phi_1 = \Phi_{l1} + \Phi_{m11} + \Phi_{m12} \tag{1}$$

$$\Phi_2 = \Phi_{m21} + \Phi_{l2} + \Phi_{m22} \tag{2}$$

where Φ_{mij} is the magnetizing flux produced by *j*th winding and links to the *i*th winding and Φ_{li} is the leakage flux of *i*th winding. The flux directions in (1) and (2) are assigned based on the winding current directions shown in Fig. 3(a) with red lines. Neglecting the saturation of the core, the system is linear. Therefore, magnetizing fluxes can be expressed as [27]

$$\Phi_{m11} = \frac{N_1 I_1}{4R_T}\ ,\ \Phi_{m12} = \frac{N_2 I_2}{4R_T}\ ,\ \Phi_{m21} = \frac{N_1 I_1}{4R_T}$$
$$\Phi_{m22} = \frac{N_2 I_2}{4R_T} \tag{3}$$

where R_T is the reluctance of one quadrant of the toroid core and is obtained from

$$R_T = \frac{l_{e\_T}/4}{\mu_0 \mu_{r\_T} A_{e\_T}} \tag{4}$$

where l_{e_T}, μ_{r_T}, and A_{e_T} are effective path length, relative permeability, and effective cross section of the toroid, respectively. The voltage drops on each winding in the matrix form can be expressed as

$$\begin{bmatrix} V_1 \\ V_2 \end{bmatrix} = \begin{bmatrix} r_1 & 0 \\ 0 & r_2 \end{bmatrix} \begin{bmatrix} I_1 \\ I_2 \end{bmatrix} + \frac{d}{dt} \begin{bmatrix} \lambda_1 \\ \lambda_2 \end{bmatrix} \tag{5}$$

where r_i and λ_i are the resistance and flux linkage related to *i*th winding, respectively. Since it is assumed that Φ_i links the equivalent turns of *i*th winding, the flux linkages could be obtained from:

$$\lambda_1 = N_1 \Phi_1 \tag{6}$$

$$\lambda_2 = N_2 \Phi_2 \tag{7}$$

where Φ_1 and Φ_2 are given from (1) and (2). For the conventional choke shown in Fig. 3(a), $I_p = I_1$, $I_n = I_2$, and $N_1 = N_2 = N$

by substituting the equations, the voltage drops on phase and null paths are given as

$$\begin{bmatrix} V_{p\_\text{conv}} \\ V_{n\_\text{conv}} \end{bmatrix} = \begin{bmatrix} r_1 & 0 \\ 0 & r_2 \end{bmatrix} \begin{bmatrix} I_p \\ I_n \end{bmatrix} + \begin{bmatrix} L_{l1} + \frac{N^2}{4R_T} & \frac{N^2}{4R_T} \\ \frac{N^2}{4R_T} & L_{l2} + \frac{N^2}{4R_T} \end{bmatrix} \begin{bmatrix} \frac{dI_p}{dt} \\ \frac{dI_n}{dt} \end{bmatrix} \quad (8)$$

where L_{li} is the leakage inductance of the ith winding.

Similar equations are driven to attain the voltage drops on each winding of the proposed chokes. Fig. 3(b) shows the flux linking each winding of case A. Based on the flux directions shown in this figure, the flux linking every six windings of case A can be expressed as

$$\begin{aligned}
\Phi_1 &= \Phi_{l1} + \Phi_{m11} - \Phi_{m12} + \Phi_{m13} + \Phi_{m11'} + \Phi_{m12'} + \Phi_{m13'} \\
\Phi_2 &= -\Phi_{m21} + \Phi_{l2} + \Phi_{m22} + \Phi_{m23} - \Phi_{m21'} - \Phi_{m22'} \\
&\quad + \Phi_{m23'} \\
\Phi_3 &= \Phi_{m31} + \Phi_{m32} + \Phi_{l3} + \Phi_{m33} + \Phi_{m31'} - \Phi_{m32'} \\
&\quad + \Phi_{m33'} \\
\Phi_{1'} &= \Phi_{m1'1} - \Phi_{m1'2} + \Phi_{m1'3} + \Phi_{l1'} + \Phi_{m1'1'} + \Phi_{m1'2'} \\
&\quad + \Phi_{m1'3'} \\
\Phi_{2'} &= \Phi_{m2'1} - \Phi_{m2'2} - \Phi_{m2'3} + \Phi_{m2'1'} + \Phi_{l2'} + \Phi_{m2'2'} \\
&\quad - \Phi_{m2'3'} \\
\Phi_{3'} &= \Phi_{m3'1} + \Phi_{m3'2} + \Phi_{m3'3} + \Phi_{m3'1'} - \Phi_{m3'2'} + \Phi_{l3'} \\
&\quad + \Phi_{m3'3'}. \qquad (9)
\end{aligned}$$

Considering the linear system (avoiding core saturation), the magnetizing flux in the abovementioned equation can be obtained from the equivalent electric circuit of the proposed choke, which is shown in Fig. 4(a). In the figure, the leakage fluxes of the windings are not shown for simplification. The winding EMFs, the reluctance of one quadrant of the toroid core, the air gap reluctance, and the reluctance of the half of the solenoid core are analogous to the voltage sources R_T, R_g, and R_S, respectively. R_g and R_S are calculated from

$$R_S = \frac{l_{e\_S}}{\mu_0 \mu_{r\_S} A_{e\_S}}, R_g = \frac{l_{e\_g}}{\mu_0 A_{e\_g}} \quad (10)$$

where l_{e_S}, μ_{r_S}, and A_{e_S} are, respectively, effective path length, relative permeability, and effective cross section of the solenoid, and l_{e_g} and A_{e_g} are, respectively, the effective path length and effective cross section of the air gap between toroid and solenoid cores.

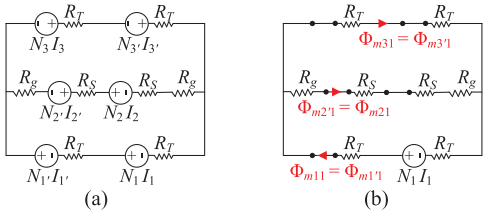

Fig. 4. (a) Equivalent electric circuit of the proposed choke. (b) Equivalent circuit for calculating Φmi1.

To attain the Φ_{mij}, it is enough to zero all voltage sources except $N_j I_j$ and then calculate the Φ_{mij} from circuit theory. For instance, the equivalent circuit for calculating the Φ_{mi1} is shown in Fig. 4(b). In the figure, the magnetizing fluxes are shown with red color, which can be calculated by solving the circuit. Therefore, all magnetizing fluxes in (9) are attained. Similar to (6) and (7), the flux linkages of windings in case A are given as

$$\lambda_i = N_i \Phi_i \ , \ i \in \left[1\ 2\ 3\ 1'\ 2'\ 3'\right]. \quad (11)$$

As a result, the voltage drops of all winding of case A can be obtained as where

$$\begin{aligned}
&R_{C1} = 2R_T + \frac{R_T \times (2R_g + 2R_S)}{R_g + R_T + R_S}, \ R_{C2} = 4R_S + 4R_g + 2R_T \\
&R_{C3} = R_{C1} \times \frac{R_T + R_S + R_g}{R_g + R_S}, \ R_{C4} = R_{C1} \times \frac{R_T + R_S + R_g}{R_T} \\
&R_{C5} = 2R_S + 2R_g + R_T. \qquad (13)
\end{aligned}$$

The flux linking each winding of case B and case C are shown in Fig. 3(c) and (d), respectively. From these figures, the flux directions are the same as those of case A. However, the voltage drops on the windings in cases B and C are equal to case A. In the other word, the resulted voltages in (12), as shown at the bottom of this page, are also referred to cases B and C. The last step is to calculate the voltage drops on the phase and null paths in our proposed chokes. From Fig. 3(b), for case A, it gives

$$I_1 = I_2 = I_3 = I_p \ , \ I_{1'} = I_{2'} = I_{3'} = I_n \quad (14)$$

$$V_{p\_A} = V_1 + V_2 + V_3 \ , \ V_{n\_A} = V_{1'} + V_{2'} + V_{3'}. \quad (15)$$

$$\begin{bmatrix} V_1 \\ V_2 \\ V_3 \\ V_{1'} \\ V_{2'} \\ V_{3'} \end{bmatrix} = \begin{bmatrix} r_T & 0 & 0 & 0 & 0 & 0 \\ 0 & r_S & 0 & 0 & 0 & 0 \\ 0 & 0 & r_T & 0 & 0 & 0 \\ 0 & 0 & 0 & r_T & 0 & 0 \\ 0 & 0 & 0 & 0 & r_S & 0 \\ 0 & 0 & 0 & 0 & 0 & r_T \end{bmatrix} \begin{bmatrix} I_1 \\ I_2 \\ I_3 \\ I_{1'} \\ I_{2'} \\ I_{3'} \end{bmatrix} + \begin{bmatrix} L_{l1} + \frac{N_T^2}{R_{C1}} & -\frac{N_T N_S}{R_{C2}} & \frac{N_T^2}{R_{C3}} & \frac{N_T^2}{R_{C1}} & \frac{N_T N_S}{R_{C2}} & \frac{N_T^2}{R_{C3}} \\ -\frac{N_T N_S}{R_{C4}} & L_{l2} + \frac{N_S^2}{R_{C5}} & \frac{N_T N_S}{R_{C4}} & -\frac{N_T N_S}{R_{C4}} & -\frac{N_S^2}{R_{C5}} & \frac{N_T N_S}{R_{C4}} \\ \frac{N_T^2}{R_{C3}} & \frac{N_T N_S}{R_{C2}} & L_{l3} + \frac{N_T^2}{R_{C1}} & \frac{N_T^2}{R_{C3}} & -\frac{N_T N_S}{R_{C2}} & \frac{N_T^2}{R_{C1}} \\ \frac{N_T^2}{R_{C1}} & -\frac{N_T N_S}{R_{C2}} & \frac{N_T^2}{R_{C3}} & L_{l1'} + \frac{N_T^2}{R_{C1}} & \frac{N_T N_S}{R_{C2}} & \frac{N_T^2}{R_{C3}} \\ \frac{N_T N_S}{R_{C4}} & -\frac{N_S^2}{R_{C5}} & -\frac{N_T N_S}{R_{C4}} & \frac{N_T N_S}{R_{C4}} & L_{l2'} + \frac{N_S^2}{R_{C5}} & -\frac{N_T N_S}{R_{C4}} \\ \frac{N_T^2}{R_{C3}} & \frac{N_T N_S}{R_{C2}} & \frac{N_T^2}{R_{C1}} & \frac{N_T^2}{R_{C3}} & -\frac{N_T N_S}{R_{C2}} & L_{l3'} + \frac{N_T^2}{R_{C1}} \end{bmatrix} \begin{bmatrix} \frac{dI_1}{dt} \\ \frac{dI_2}{dt} \\ \frac{dI_3}{dt} \\ \frac{dI_{1'}}{dt} \\ \frac{dI_{2'}}{dt} \\ \frac{dI_{3'}}{dt} \end{bmatrix} \quad (12)$$

Substituting the abovementioned equations in (12) yields the voltage drops on phase and null paths, which refer to case A as

$$\begin{bmatrix} V_{p\_A} \\ V_{n\_A} \end{bmatrix} = \begin{bmatrix} 2r_T + r_S & 0 \\ 0 & 2r_T + r_S \end{bmatrix} \begin{bmatrix} I_p \\ I_n \end{bmatrix} + \begin{bmatrix} L_{l1}+L_{l2}+L_{l3}+\frac{N_T^2}{R_T}+\frac{N_S^2}{R_{C5}} & \frac{N_T^2}{R_T}-\frac{N_S^2}{R_{C5}} \\ \frac{N_T^2}{R_T}-\frac{N_S^2}{R_{C5}} & L_{l1'}+L_{l2'}+L_{l3'}+\frac{N_T^2}{R_T}+\frac{N_S^2}{R_{C5}} \end{bmatrix} \times \begin{bmatrix} \frac{dI_p}{dt} \\ \frac{dI_n}{dt} \end{bmatrix} \tag{16}$$

where, from (13), it can be shown that

$$\frac{2}{R_{C1}} + \frac{2}{R_{C3}} = \frac{1}{R_T}. \tag{17}$$

Considering case B shown in Fig. 3(c), the currents and voltages of the winding are

$$I_1 = I_2 = I_{3'} = I_p \ , \ \ I_{1'} = I_{2'} = I_3 = I_n \tag{18}$$

$$V_{p\_B} = V_1 + V_2 + V_{3'} \ , \ \ V_{n\_B} = V_{1'} + V_{2'} + V_3. \tag{19}$$

Therefore, similar to (16), the voltage drops on the phase and null paths refer to case B, which can be obtained as

$$\begin{bmatrix} V_{p\_B} \\ V_{n\_B} \end{bmatrix} = \begin{bmatrix} 2r_T + r_S & 0 \\ 0 & 2r_T + r_S \end{bmatrix} \begin{bmatrix} I_p \\ I_n \end{bmatrix} + \begin{bmatrix} L_{l1}+L_{l2}+L_{l3'}+\frac{N_T^2}{R_T}+\frac{N_S^2}{R_{C5}} & \frac{N_T^2}{R_T}-\frac{N_S^2}{R_{C5}} \\ \frac{N_T^2}{R_T}-\frac{N_S^2}{R_{C5}} & L_{l1'}+L_{l2'}+L_{l3}+\frac{N_T^2}{R_T}+\frac{N_S^2}{R_{C5}} \end{bmatrix} \times \begin{bmatrix} \frac{dI_p}{dt} \\ \frac{dI_n}{dt} \end{bmatrix}. \tag{20}$$

From Fig. 3(d), the currents and voltages of the windings in case C are

$$I_{1'} = I_{2'} = I_1 = I_p \ , \ \ I_{3'} = I_2 = I_3 = I_n \tag{21}$$

$$V_{p\_C} = V_{1'} + V_{2'} + V_1 \ , \ \ V_{n\_C} = V_{3'} + V_2 + V_3. \tag{22}$$

However, similarly, it gives

$$\begin{bmatrix} V_{p\_C} \\ V_{n\_C} \end{bmatrix} = \begin{bmatrix} 2r_T + r_S & 0 \\ 0 & 2r_T + r_S \end{bmatrix} \begin{bmatrix} I_p \\ I_n \end{bmatrix} + \begin{bmatrix} L_{11\_C} & L_{12\_C} \\ L_{21\_C} & L_{22\_C} \end{bmatrix} \begin{bmatrix} \frac{dI_p}{dt} \\ \frac{dI_n}{dt} \end{bmatrix} \tag{23}$$

where

$$\begin{aligned} L_{11\_C} &= L_{l1'} + L_{l2'} + L_{l1} + \left(\frac{4N_T^2}{R_{C1}}\right) + \left(\frac{2}{R_{C2}} + \frac{2}{R_{C4}}\right) \times N_T N_S + \left(\frac{N_S^2}{R_{C5}}\right) \\ L_{12\_C} &= L_{21\_C} = \left(\frac{4N_T^2}{R_{C3}}\right) - \left(\frac{2}{R_{C2}} + \frac{2}{R_{C4}}\right) \times N_T N_S - \left(\frac{N_S^2}{R_{C5}}\right) \\ L_{22\_C} &= L_{l3'} + L_{l2} + L_{l3} + \left(\frac{4N_T^2}{R_{C1}}\right) + \left(\frac{2}{R_{C2}} + \frac{2}{R_{C4}}\right) \times N_T N_S + \left(\frac{N_S^2}{R_{C5}}\right). \end{aligned} \tag{24}$$

B. CM Inductance

The CM noise current $I_{\rm CM}$ flows equally form phase and null paths in the same direction from the noise source to the EMI filter and comes back through the ground path in the single-phase grounded system. This current generates an equal voltage drop on the phase and null windings of the EMI choke, which is named CM voltage $V_{\rm CM}$. Thus, to analyze the CM performance of the EMI choke we have

$$I_{p\_\rm CM} = I_{n\_\rm CM} = I_{\rm CM}/2 \tag{25}$$

$$V_{p\_\rm CM} = V_{n\_\rm CM} = V_{\rm CM} \tag{26}$$

where I_{p_CM} and I_{n_CM} are, respectively, phase and null currents of the choke, and V_{p_CM} and V_{n_CM} are its phase and null voltages, respectively. Neglecting winding resistances, in [28], the CM inductance $L_{\rm CM}$ is defined as

$$L_{\rm CM} = \frac{V_{\rm CM}}{dI_{\rm CM}/dt}. \tag{27}$$

Substituting (25) and (26) in (8) yields the CM-phase voltage of the conventional choke as

$$V_{\rm CM\_conv} = \frac{r_1 I_{\rm CM}}{2} + \left(\frac{L_{l1}}{2} + \frac{N^2}{4R_T}\right)\frac{dI_{\rm CM}}{dt}. \tag{28}$$

Therefore, the CM inductance of the conventional choke is obtained as

$$L_{\rm CM\_conv} = \frac{V_{\rm CM\_conv}}{dI_{\rm CM}/dt} = \frac{L_{l1}}{2} + \frac{N^2}{4R_T} \cong \frac{N^2}{4R_T} \tag{29}$$

where the leakage inductance of the winding is neglected comparing to the second term. Also from (16), the CM-phase voltage of case A is determined as

$$V_{\rm CM\_A} = \frac{(2r_T + r_S)}{2} I_{\rm CM} + \left(\frac{L_{l1} + L_{l2} + L_{l3}}{2} + \frac{N_T^2}{R_T}\right)\frac{dI_{\rm CM}}{dt}. \tag{30}$$

However, the CM inductance of case A is

$$L_{\rm CM\_A} = \frac{L_{l1} + L_{l2} + L_{l3}}{2} + \frac{N_T^2}{R_T} \cong \frac{N_T^2}{R_T}. \tag{31}$$

Similarly, the CM inductances of cases B and C are determined as

$$L_{\rm CM\_B} = \frac{L_{l1} + L_{l2} + L_{l3'}}{2} + \frac{N_T^2}{R_T} \cong \frac{N_T^2}{R_T} \tag{32}$$

$$L_{\rm CM\_C} = \frac{L_{l1'} + L_{l2'} + L_{l1}}{2} + \frac{N_T^2}{R_T} \cong \frac{N_T^2}{R_T}. \tag{33}$$

Comparing the calculated CM inductances in (31)–(33) with the inductance of the conventional choke in (29) shows that for $N_T = N/2$, we have $L_{\rm CM\_conv} = L_{\rm CM\_A} = L_{\rm CM\_B} = L_{\rm CM\_C}$. In other words, by proper design of the windings on the toroid, the CM inductances of all chokes could be equal. As a result, the proposed choke does not affect the CM inductance, which is desired in this article.

C. DM Inductance

The DM current $I_{\rm DM}$ flows through the phase and null paths of the EMI choke in the opposite directions. Therefore, the DM phase and null currents and voltages of an EMI choke are determined as

$$I_{p\_\rm DM} = -I_{n\_\rm DM} = I_{\rm DM} \tag{34}$$

$$V_{p\_\rm DM} = -V_{n\_\rm DM} = V_{\rm DM} \tag{35}$$

where I_{p_DM} and I_{n_DM} are, respectively, the phase and the null currents of the choke, and V_{p_DM} and V_{n_DM} are its phase and null voltages, respectively. The DM inductance is determined from [28]

$$L_{\rm DM} = \frac{V_{\rm DM}}{dI_{\rm DM}/dt}. \tag{36}$$

Substituting (34) and (35) in (8) yields the DM phase voltage of the conventional choke as

$$\begin{aligned} V_{\rm DM\_conv} &= r_1 I_{\rm DM} + (L_{l1})\,\frac{dI_{\rm DM}}{dt} \\ &= r_1 I_{\rm DM} + (L_{l\_\rm conv})\,\frac{dI_{\rm DM}}{dt} \end{aligned} \tag{37}$$

where L_{l_conv} is the leakage inductance of each winding of the conventional choke. Considering (36), the inductance of the conventional choke is obtained as

$$L_{\rm DM\_conv} = L_{l\_\rm conv}. \tag{38}$$

Previous works have been done to model the leakage inductance L_{l_conv} [29] and [28]. Assuming a high-permeability toroid core, this inductance approximately is just the function of the toroid geometry and number of turns and is independent of the core material [29]. To attain the leakage inductance, the phase winding shown in Fig. 3(a) is modeled as a wound on a rod. This leading to the inductance of

$$L_{\rm DM\_conv} = L_{l\_\rm conv} \cong 2.5\ \mu_0 N^2 \frac{A_e}{l_{\rm eff}} \left(\frac{l_e}{2}\sqrt{\frac{\pi}{A_e}}\right)^{1.45} \tag{39}$$

where A_e is the core cross section, l_e is the mean path length of the toroid, and $l_{\rm eff}$ is the effective mean path length of the leakage flux Φ_{l1}. Based on the empirical formula given in [28], the $l_{\rm eff}$ can be calculated as

$$l_{\rm eff} = \sqrt{\frac{\rm OD^2}{\sqrt{2}}\left(\frac{\theta}{4} + 1 + \sin\frac{\theta}{2}\right)^2 + \rm ID^2\left(\frac{\theta}{4} - 1 + \sin\frac{\theta}{2}\right)^2} \tag{40}$$

where OD and ID are the external and internal diameters of the toroid, respectively, and θ is the angle covered by each winding.

Considering the DM currents in case A, Substituting (34) and (35) in (16) yields the DM phase voltage and consequently the DM inductance as

$$\begin{aligned} V_{\rm DM\_A} =\ & (2r_T + r_S)\, I_{\rm DM} \\ & + \left(L_{l1} + L_{l2} + L_{l3} + \frac{2N_S^2}{R_{C5}}\right)\frac{dI_{\rm DM}}{dt} \end{aligned} \tag{41}$$

$$L_{\rm DM\_A} = L_{l1} + L_{l2} + L_{l3} + \frac{2N_S^2}{R_{C5}} \cong 2L_{l\_T} + \frac{2N_S^2}{R_{C5}} \tag{42}$$

where L_{l_T} is the leakage inductance of each winding on toroid and the leakage inductance of the winding on the solenoid is neglected for simplification. L_{l_T} can be determined similar to (39). Therefore, the DM inductance of case A is obtained as

$$L_{\rm DM\_A} \cong 5\ \mu_0 N_T^2 \frac{A_e}{l_{\rm eff}} \left(\frac{l_e}{2}\sqrt{\frac{\pi}{A_e}}\right)^{1.45} + \frac{2N_S^2}{R_{C5}} \tag{43}$$

where l_e and $\rm l_{eff}$ are referred to each winding on toroid in case A.

The DM inductance of cases B and C can be determined from a similar analysis as

$$\begin{aligned} L_{\rm DM\_B} &= L_{l1} + L_{l2} + L_{l3'} + \frac{2N_S^2}{R_{C5}} \\ &\cong 5\mu_0 N_T^2 \frac{A_e}{l_{\rm eff}} \left(\frac{l_e}{2}\sqrt{\frac{\pi}{A_e}}\right)^{1.45} + \frac{2N_S^2}{R_{C5}} \end{aligned} \tag{44}$$

$$\begin{aligned} L_{\rm DM\_C} &= L_{l1'} + L_{l2'} + L_{l1} + \left(\frac{4}{R_{C1}} - \frac{4}{R_{C3}}\right) N_T^2 \\ &\quad + \left(\frac{4}{R_{C2}} + \frac{4}{R_{C4}}\right) N_T N_S + \frac{2N_S^2}{R_{C5}} \\ &\cong 5\mu_0 N_T^2 \frac{A_e}{l_{\rm eff}} \left(\frac{l_e}{2}\sqrt{\frac{\pi}{A_e}}\right)^{1.45} + \frac{2(N_S + N_T)^2}{R_{C5}}. \end{aligned} \tag{45}$$

As a result, the DM inductance of the proposed choke in all cases is increased compared to the conventional choke and can be controlled by the number of turns of the solenoid, while the CM inductance is almost constant.

D. FE Simulation

The 3-D models of the chokes are built using JMAG Designer and magnetostatic analysis is carried out. In the simulation, the toroid and solenoid cores have the relative permeability of 14 000 and 2000, respectively. The toroid in the conventional structure has 14 turns and each coil on toroid and solenoid of the proposed structure has 7 and 5 turns, respectively. The core dimensions and other conditions are constant in all simulations. Fig. 5 shows the contour plot of the magnetic flux densities with CM current of 1 mA (peak). As expected, the maximum flux density of all choke is about equal. This figure shows that there are no fluxes in the solenoid, meaning that the proposed structures do not affect the CM performance, which confirms the results in Section IV-B.

The simulated flux densities with 5 A DM excitation are shown in Fig. 6. For the conventional choke in Fig. 6(a), the DM fluxes are the leakage fluxes of the coils and their paths are prepared among the air apace around windings. For the proposed chokes of cases A and B, the magnetic paths are prepared within the solenoid, as shown in Fig. 6(b) and (c), respectively. Thus, the leakage fluxes are reduced and higher magnetic flux density is seen in the solenoid. Based on the current directions of the windings on the toroid, the flux densities in toroid are reduced and do not have symmetrical distribution. From Fig. 6(d), case C has the most maximum flux density on the solenoid. Furthermore, the distribution of toroid is symmetrical among the core. As a result, the highest DM inductance value

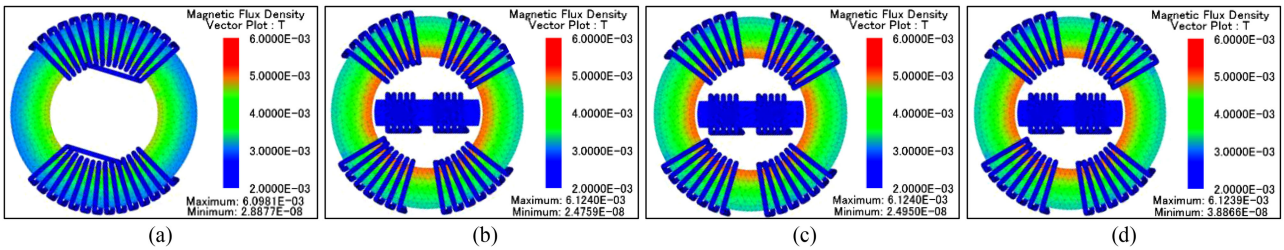

Fig. 5. FE simulation of magnetic flux density with CM current excitation. (a) Conventional choke. (b) Case A. (c) Case B. (d) Case C.

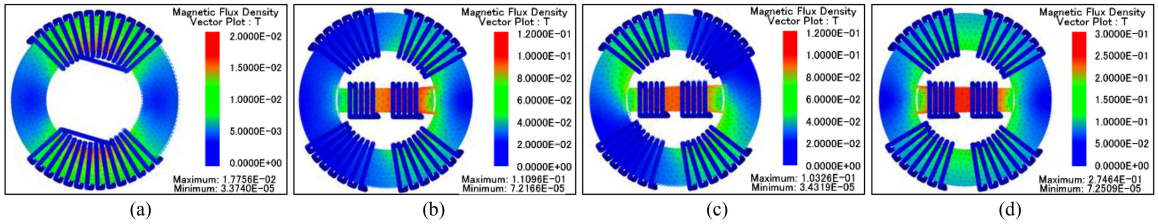

Fig. 6. FE simulation of magnetic flux density with DM current excitation. (a) Conventional choke. (b) Case A. (c) Case B. (d) Case C.

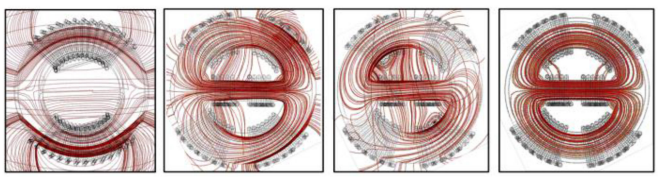

Fig. 7. FE simulation of DM magnetic flux line distributions. (a) Conventional choke. (b) Case A. (c) Case B. (d) Case C.

is expected in this case. This fact verifies the determined value of (45). Fig. 7 shows the DM magnetic flux line distributions of the chokes. For the conventional choke from Fig. 7(a), all the flux lines are propagated surrounding the core as the leakage flux. In case A and case B, the flux lines are mostly in the solenoid, but their distributions in toroid are different based on winding current directions, as can be seen from Fig. 7(b) and (c), respectively. The analysis of the DM flux line distribution of case A and B shows that these cases are different from the core leakage point of view. As can be seen, case B in Fig. 7(c) has lower leakage surrounding the core than case A in Fig. 7(b). All the flux lines of case C, as shown in Fig. 7(d), are within the cores, which lead to having the most DM inductance. The improvement in DM inductance may cause the saturation phenomenon in the cores particularly for the solenoid in our proposed chokes. The saturation limit is analyzed in the following section as a considerable parameter in designing the proposed EMI choke.

E. Saturation Analysis

The EMI choke is designed to attain an adequate inductance value in the presence of both CM and DM noises. Once the magnetic toroid core is selected for the conventional EMI choke shown in Fig 1(a), the magnetic flux density saturation limit $B_{\rm sat}$ is given from the manufacture datasheet. If the flux density in the core exceeded from $B_{\rm sat}$, then magnetic core saturation occurs. It follows that to avoid this situation for each section of the core, it must be

$$B = \frac{\Phi}{A_e} = \frac{\mu_0 \mu_r N I_m}{l_e} < B_{\rm sat} \tag{46}$$

where Φ is the net magnetic flux of the core and I_m is the winding current peak.

Both CM and DM currents may cause core saturation in the choke. For the conventional choke from (46), to avoid the saturation for the known CM current peak, the size of the core should be increased. Hence, the dimensioning of the CM inductor is due to the minimum required size to prevent the saturation phenomena. As mentioned before, the proper design of the proposed choke causes the CM inductance to be equal to one of the conventional choke. Therefore, the CM saturation conditions of the proposed choke and the conventional choke are the same. Since for some cases, like in this case study, the peak value of DM currents is quite large, the DM excitation is critical to the saturation consideration of the choke. Considering DM currents, one can rewrite (46) to attain the maximum margin of the DM inductance, as

$$L_{\rm DM} < \frac{B_{\rm sat} N A_e}{I_{\rm DM\_max}} \tag{47}$$

where $I_{\rm DM\_max}$ is the maximum DM current peak. Therefore, the DM inductance can be modified to the value given in (47) without core saturation. In other words, for a given choke, the desired value of the DM inductance is the maximum value, which could be attained from the choke while the core is not saturated. The DM inductance of the conventional choke is almost constant for the known geometry and can be calculated

from (39). If the condition of (47) is not satisfied, then another core (bigger sized) should be selected.

For the proposed chokes, the equations of DM inductance values related to different cases are presented in the previous section. Comparing the results in (43)–(45) shows that, case C has the highest inductance value. Hence, for the core saturation study, it is sufficient to analyze only case C as the worth case. The condition of (47) must be verified for both toroid and solenoid core in the proposed choke. The toroid and solenoid net fluxes (the total flux links the winding of toroid and solenoid for case C with DM current excitation) can be determined from Fig. 4(a) as

$$\Phi_{\text{net\_}T} = \frac{(N_S + N_T)\, I_{\text{DM}}}{R_{C5}} \tag{48}$$

$$\Phi_{\text{net\_}S} = \frac{2\,(N_S + N_T)\, I_{\text{DM}}}{R_{C5}}. \tag{49}$$

From (46), considering flux of (48) with the flux caused by leakage inductance attains the condition for the toroid core to be nonsaturated as

$$B_T = \frac{\Phi_{\text{net\_}T}}{A_{e\_T}} = \frac{(N_S + N_T)\, I_{\text{DM\_max}}}{A_{e\_T} R_{C5}} + \frac{2 L_{l\_T} I_{\text{DM\_max}}}{N_T A_{e\_T}} < B_{\text{sat\_}T}. \tag{50}$$

Similarly, for the solenoid core from (46) and (49), the condition is obtained as

$$B_S = \frac{\Phi_{\text{net\_}S}}{A_{e\_S}} = \frac{2\,(N_S + N_T)\, I_{\text{DM\_max}}}{A_{e\_S} R_{C5}} < B_{\text{sat\_}S}. \tag{51}$$

The number of turns of solenoid winding N_S can be the parameter in (50) and (51), which avoids the saturation of the cores. Therefore, the saturation phenomenon is considered in the design phase of the proposed choke. Considering the toroid core, N_S is determined from (50) as

$$N_S < \frac{B_{\text{sat\_}T} A_{e\_T} R_{C5}}{I_{\text{DM\_max}}} - \frac{2 L_{l\_T} R_{C5}}{N_T} - N_T. \tag{52}$$

Also for the solenoid core, from (51), N_S is obtained to be

$$N_S < \frac{B_{\text{sat\_}S} A_{e\_S} R_{C5}}{2 I_{\text{DM\_max}}} - N_T. \tag{53}$$

The selected N_S must verify both conditions in (52) and (53). According to (45), the DM inductance of case C increases as the N_S is increased. Therefore, to attain more DM inductance value, it is desired to select the maximum number of turns N_S, which satisfies both (52) and (53). Moreover, the term R_{C5} (which is a function of μ_{r_S}) shows the dependence of the limiting conditions to the core material. In other words, the proper material selection of the solenoid core is another degree of freedom to prevent saturation. For instance, if the maximum value of N_S from (52) and (53) becomes lower than 1, then using the solenoid core with lower μ_{r_S} is suggested. Similar equations can be driven to attain the conditions for N_S in cases A and B to prevent saturation. For a more detailed analysis of the core saturation, finite element modeling can be helpful [30]. As a result, the proposed choke can be considered as a linear system, because its CM performance is similar to the conventional choke and also its DM performance is linear by the proper design of air-gap and the number of turn of the solenoid.

TABLE I
PARAMETERS OF THE MAGNETIC CORES

	Toroidal Core	Solenoid Core
Material	Mn-Zn	Mn-Zn (N87)
Dimension	OD = 38 (mm) ID = 22 (mm) H = 15 (mm)	L = 21 (mm) W = 8 (mm) H = 15 (mm)
	$A_{e\_T} = H \times (OD\text{-}ID)/2$ $l_{e\_T} = \pi \times (OD+ID)/2$	$A_{e\_S} = H \times W$ $l_{e\_S} = L/2$ $A_{e\_g} \approx 1.2 \times A_{e\_S}$ $l_{e\_g} \approx 0.5$ (mm)
Inductance ratio A_L	23 ($\mu H/N^2$)	-
Relative Permeability	μ_{r_T} = 14600	μ_{r_S} = 2200
Saturation Level (25 °C)	0.38 (T)	0.45 (T)

IV. EXPERIMENTAL RESULTS AND DISCUSSION

To verify and compare the results, three chokes with the structures shown in Fig. 2 and a corresponding conventional choke are built. The core material and their dimensions are the same in all chokes. The physical parameters of the magnetic cores are presented in Table I, the Mn–Zn materials are used for both toroid and solenoid cores. The dimension of the toroid is selected based on the manufacturing catalog. The length of the solenoid core is 1 mm less than the internal diameter of the toroidal core resulting in two 0.5 mm air gap lengths ($l_{e\_g} = 0.5\,\text{mm}$). The inductance ratio of the toroid, the saturation level, and relative permeability of the cores are also described in Table I.

To evaluate the performance of the proposed choke and verify the analytical discussions of the previous section, different measurements have been done with the fabricated chokes. The CM and DM inductances of the chokes are measured. Then the chokes are mounted in the PCB board of an EMI filter to measure the DM and CM insertion losses (ILs), and finally the in-circuit performance of the filters is tested in a 750-W induction motor drive system.

A. CM and DM Impedance

The required CM inductance of an EMI choke is specified based on the power converter requirements to filter the CM emissions. This value is 4.5 mH in this article. Thus, based on the inductance ratio given in Table I, the number of turns of the conventional choke N is calculated to be 14 turns for each winding. For the proposed choke based on the presented analysis, N_T is selected one half of N to attain the same CM inductance value. As mentioned in Section III, N_S is the design parameter to avoid core saturation caused by DM currents. The maximum margins of N_S are given from (52) and (53) for the parameters given in Table I, $N_T = 7$ and $I_{\text{DM\_}max} = 12\text{A}$ as $N_S < 13.54$ and $N_S < 5.6$, respectively. Thus, to prevent saturation, N_S is selected equal to 5. The specifications of the fabricated chokes are described in Table II. The homogeneous copper wire is used for all windings and the total occupied space of the chokes is equal. The CM and DM inductances of the built chokes are measured using a typical *RLC* meter at 10 kHz.

TABLE II
SPECIFICATIONS OF THE FABRICATED CHOKES

	Conventional choke	Proposed choke Case A	Proposed choke Case B	Proposed choke Case C
Total toroid number of turns	2 × 14 (N = 14)	4 × 7 (N_T = 7)	4 × 7 (N_T = 7)	4 × 7 (N_T = 7)
Total solenoid number of turns	–	2 × 5 (N_S = 5)	2 × 5 (N_S = 5)	2 × 5 (N_S = 5)
Occupied Space	12.54 cm^3	12.54 cm^3	12.54 cm^3	12.54 cm^3
Wire Diameter	0.9 mm	0.9 mm	0.9 mm	0.9 mm
Wire Length	111 cm	124 cm	124 cm	124 cm
Wire Copper Resistance	r_1= r_2=31mΩ	$2r_T$+r_S=35mΩ	$2r_T$+r_S=35mΩ	$2r_T$+r_S=35mΩ

TABLE III
CM AND DM INDUCTANCES MEASURED AT 10 kHz

Choke Type	Measured L_{CM}	Calculated L_{CM}	Measured L_{DM}	Calculated L_{DM}
Conventional	4.56 mH	4.57 mH from (29)	9.28 μH	8.08 μH from (39)
Case A	4.56 mH	4.57 mH from (31)	12.44 μH	10.76 μH from (43)
Case B	4.55 mH	4.57 mH from (32)	12.16 μH	10.76 μH from (44)
Case C	4.59 mH	4.57 mH from (33)	51.22 μH	53.26 μH from (45)

The measure inductances are compared with their calculated values presented in Section III, as described in Table III. The CM inductance is measured while the phase and null windings are connected in parallel. The measured $L_{\rm CM}$ of all chokes is around its calculated value and its desired value, which is 4.5 mH. The measured values show that the proposed choke does not affect the CM inductance and verified the analysis presented in the previous section. For the measurement of the DM inductance, the output of the phase winding is connected to the output of the null winding, and the inductance between phase and null inputs is measured which is $2L_{\rm DM}$. The measured $L_{\rm DM}$ of the chokes is compared with its related calculated value. As listed in Table III, the measured values are around the predicted values. As expected, the DM inductance is modified in the proposed cases and case C has the maximum value. These measurements verify the theoretical analysis presented in Section III at a low frequency.

To analyze the performance of the chokes over the frequency range (150 kHz to 30 MHz), the CM and DM impedances have been measured using the Agilent N9917A-210 vector network analyzer (VNA). In a typical one-port system, the measured S-parameters of VNA can be converted to the Z-parameters using [31]

$$Z = Z_0 \frac{1 + S_{11}}{1 - S_{11}} \tag{54}$$

where Z_0 is 50 Ω reference impedance. The experimental CM and DM impedance measurement configurations are presented in [32]. Fig. 8(a) and (b) shows the required terminal connections to measure the CM and DM impedances, respectively. The measured impedances are shown in Fig. 9. Fig. 9(a) shows the absolute value and phase of the CM impedances from 150 kHz to 30 MHz. As expected, the CM impedances of all chokes are almost equal over the range, which is desired in this work. The

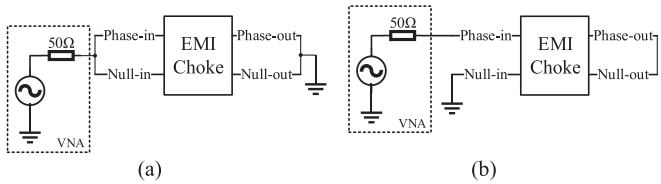

Fig. 8. Experimental impedance measurement configuration using VNA. (a) CM. (b) DM.

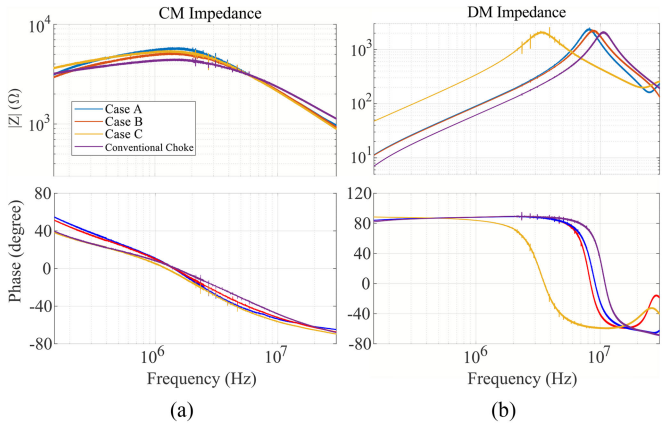

Fig. 9. Measured impedance of the chokes. (a) CM impedance. (b) DM impedance.

measured DM impedance is shown in Fig. 9(b). As expected, at the frequencies below 3 MHz, the impedance of the proposed choke with case C structure is much higher than the others. This is because the low-frequency impedance of the EMI choke is mainly dominated by its DM inductance [18]. For the frequencies above 3 MHz, the capacitance of the choke decreases the impedance characteristic due to the parallel resonance. The value of EPC can be obtained from

$$\text{EPC} = \frac{1}{(2\pi f_c)^2 L_{\rm DM}} \tag{55}$$

where f_c is the resonant frequency that the phase is zero. From Fig. 9(b), the calculated EPCs are 40.8 pF for case C and 23 pF for the conventional choke. Increasing the capacitance makes the DM impedance of the proposed choke to be less than the impedance of conventional choke in the range of 7 MHz to near 25 MHz. However, the grounding methods, the coupling effects of the filter components, and the interaction with source impedance usually play dominant roles for EMI noise rejection performance in the high-frequency range [33]. Therefore, the resonance of the proposed choke may not much affect the filtering performance in the high-frequency range. Furthermore, higher DM inductance of the proposed choke attains better noise rejection at low frequencies, which is important to reduce the size of the filter.

From (45), the DM inductance of case C is the function of a designable parameter N_S, which is selected to have the maximum inductance value without core saturation. To validate this, the DM impedances of case C are also measured using VNA, for $N_S = 4$ and $N_S = 3$ which are shown in Fig. 10.

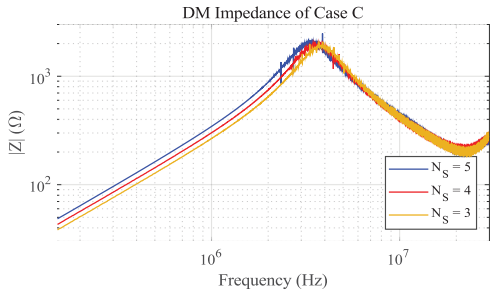

Fig. 10. Measured DM impedance of case C with different N_S.

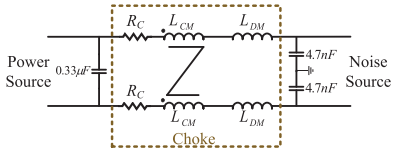

Fig. 11. Circuit diagram of the EMI filter.

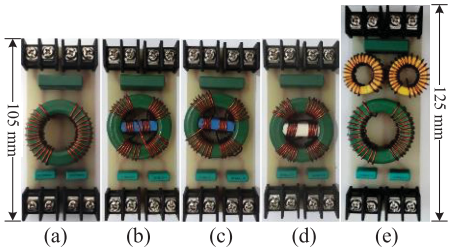

Fig. 12. Fabricated EMI filters includes the following. (a) Conventional choke. (b) Choke with case A structure. (c) Choke with case B structure. (d) Choke with case C structure. (e) Conventional choke with two additional DM inductors.

From the figure, the low-frequency DM impedance is increased as N_S increases. These measurements validate the predicted DM inductance of case C in (45).

B. Insertion Loss Measurement

To compare the presented chokes in the previous section, five EMI filters with different chokes are built based on the circuit model shown in Fig. 11. The $L_{\rm CM}$ and $L_{\rm DM}$ are the CM and DM inductances of the choke and R_C is the conduction resistance of the choke wire. This model works as a *CL*- and *LC*-filter for common and differential modes, respectively, [4]. Fig. 12 shows the fabricated filters. Although these filters are not optimum volume designed, they are suitable for comparing the chokes in the same PCB and the same conditions. The filter in Fig. 12(e) consists of a conventional choke with two series of 40.5 μH additional iron-powder inductors. Based on the measured DM inductance values in Table III, these two additional inductors compensate for the difference of DM inductance between case C and the conventional EMI filter. However, the size of this filter has been increased near to 20%.

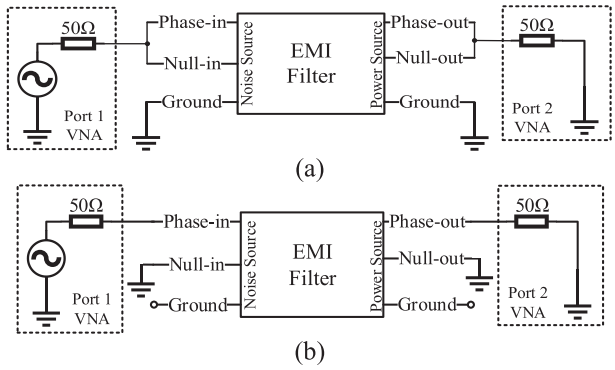

Fig. 13. Experimental configuration to measure (a) CM and (b) DM, IL using two-port VNA.

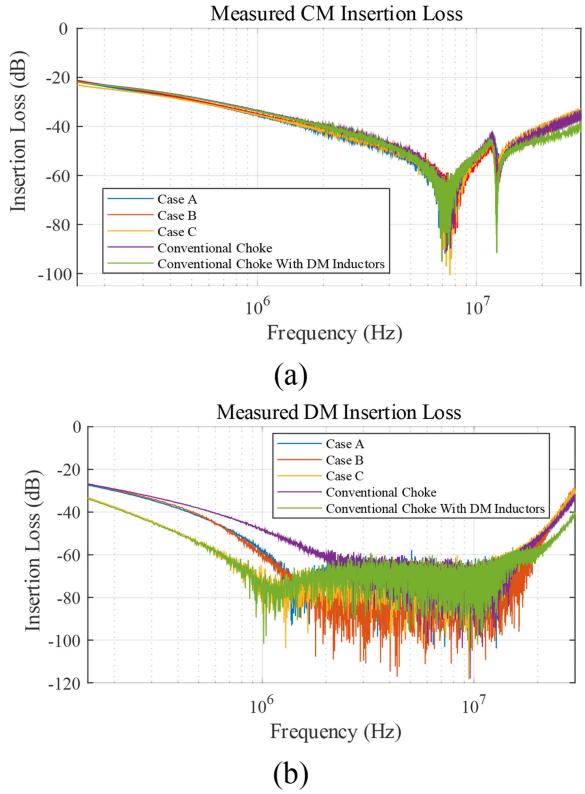

Fig. 14. Measured IL of the filters (a) CM IL and (b) DM IL.

To evaluate the filter noise rejection performance, the IL of the transmission line is considered. The lowering IL value causes increasing noise rejection [34]. Fig. 13(a) and (b) shows the experimental IL measurement configurations for both common and differential modes. The measurement results of the CM IL in Fig. 14(a) validate the same CM IL for all filters in Fig. 12. Fig. 14(b) illustrates the DM ILS. The proposed filter with a choke of case C (yellow curve) has the minimum value of IL at frequencies under 3 MHz. The results in Fig. 14(b) show that the filter of Fig. 12(e), with two additional DM inductors, has the IL (green curve) similar to the proposed filter of case C, which means that these filters have similar DM noise rejection performance.

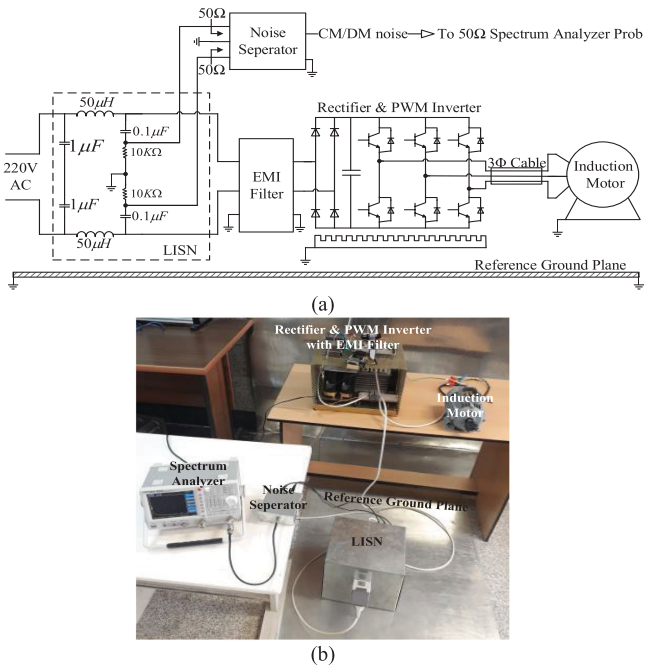

Fig. 15. Experimental setup to measure conducted EMI noise of the three-phase induction motor drive. (a) System block diagram. (b) Laboratory setup.

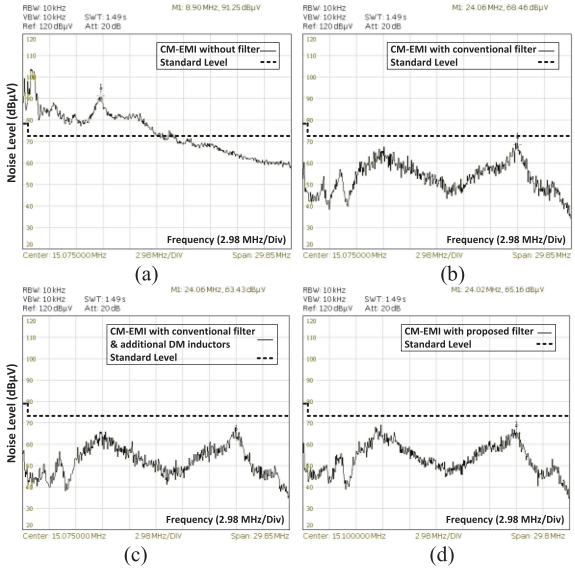

Fig. 16. Experimental results of the conducted CM noise measurement of the system. (a) Without filter. (b) With conventional filter. (c) With the proposed filter (case C). (d) With the conventional filter including two DM inductors.

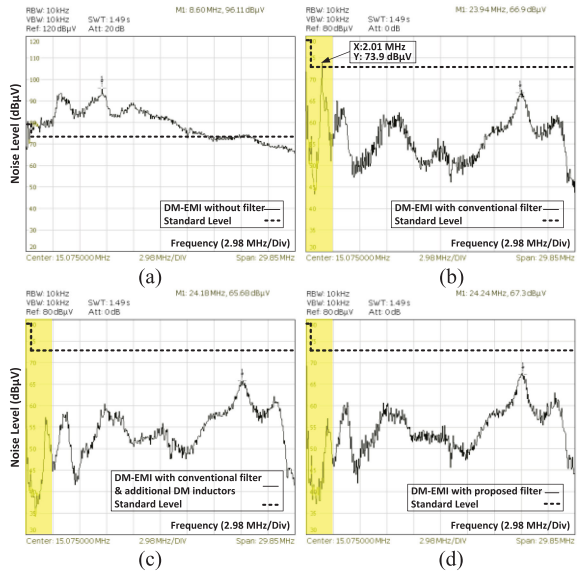

Fig. 17. Experimental results of the conducted DM noise measurement of the system. (a) Without filter. (b) With conventional filter. (c) With the proposed filter (case C). (d) With the conventional filter including two DM inductors.

C. Conducted EMI Results

The in-circuit performance of the filters has been tested with a 750-W laboratory induction motor drive system. The circuit diagram of the fabricated system to measure the conducted EMI is shown in Fig. 15(a). It consists of a built EMI filter connected to the ac/dc/ac converter, which feeds a three-phase induction motor. The inverter works with its nominal voltage and is controlled with sinusoidal PWM comes from the TMS320F2812 DSP unit. A fabricated line impedance stabilization network and a noise separator are utilized to measure the conducted CM and DM noises of the system [35]. The photograph of the laboratory setup is shown in Fig. 15(b). The Hameg HMS-1010 spectrum analyzer is used to capture the quasi-peak noise spectra according to the CISPR-22 EMC standard. It can be seen that case C has the maximum DM inductance; therefore, only the filter containing the choke with the structure of case C is used. The screenshot of the measured CM noise spectra of the system from 150 kHz to 30 MHz with the quasi-peak standard noise level is shown in Fig. 16. Fig. 16(a) represents the CM EMI of the system without a filter. As can be seen, the measured noise is over the standard limit in the frequencies below 15 MHz. Fig. 16(b) shows that the CM noise of the system with the conventional filter passes the standard limit. Fig. 16(c) and (d) shows that the CM noise of the system with the proposed filter and conventional choke with extra DM inductors are similar. That means, the proposed choke used in the filter does not affect the CM performance.

The measured DM noise level of the system without the filter is illustrated in Fig. 17(a), which is over the limit. The DM noise spectra using a conventional filter are presented in Fig. 17(b). As mentioned in Section IV (A), the DM impedance of the conventional choke is relatively low at frequencies below 3 MHz; thus, the measured DM noise is not properly filtered in this range and reached to the standard level at frequencies below 3 MHz (the yellow shaded region on screen). Fig. 17(c) shows the DM noise of the system with the proposed filter, which has reduced the DM noise level up to 16 dB at frequencies below 3 MHz by increasing the low-frequency DM inductance. Fig. 17(d) represents the DM noise of the filter with conventional choke and extra DM inductors. The measured spectra show that these two filters are similar in DM performance. From Table II, the wire length of the proposed choke is about 11% more than the conventional and consequently, the conduction loss becomes more. However, the proposed choke has a lower wire length compared to the conventional filter with additional

DM inductors. Therefore, the Ohmic per-phase resistance of the proposed filter is lower than the conventional filter with DM inductors while the performances are the same. Therefore, the proposed choke has an improvement in filter efficiency from this point of view.

As a result, the in-circuit DM and CM performances of the proposed filter are similar to the performances of the filter shown in Fig. 12(e), while the size of the filter is reduced near to 20%.

V. Conclusion

This article presented an integrated EMI choke with improved DM performance. An analysis is presented based on the magnetic field distributions in the different configurations. The derived equations show that the CM inductance of the proposed choke is almost equal to the one of conventional choke, while the DM inductance of the proposed choke is increased by making the proper path for leakage fluxes and designing solenoid core. The equations are presented, which predict the DM inductance of the proposed chokes for different cases. The analytical results are evaluated by experimental measurements. The measured DM impedance and ILs of the fabricated choke with the proposed structure show the significant increase in DM inductance. Finally, the in-circuit performance of the proposed choke is tested. The experimental results of the conducted EMI reveal the good performance of the proposed choke in the noise rejection, while it reduces the filter size by about 20%.

References

[1] M. Moreau, N. Idir, and P. L. Moigne, "Modeling of conducted EMI in adjustable speed drives," *IEEE Trans. Electromagn. Compat.*, vol. 51, no. 3, pp. 665–672, Aug. 2009.

[2] *Industrial, Scientific and Medical Radio-Frequency Equipment Electromagnetic Disturbance Characteristics Limits and Methods of Measurement*, CISPR11 Edition 5.0, 2009–2005.

[3] *Electromagnetic Compatibility (EMC)—Part 4–6: Testing and Measurement Techniques—Immunity to Conducted Disturbances, Induced by Radio-Frequency Fields*, IEC 61000 Edition 3.0, 2008–2010.

[4] F. Y. Shih, D. Y. Chen, Y. P. Wu, and Y. T. Chen, "A procedure for designing EMI filters for AC line applications," *IEEE Trans. Power Electron.*, vol. 11, no. 1, pp. 170–181, Jan. 1996.

[5] S. Wang, Y. Y. Maillet, F. Wang, D. Boroyevich, and R. Burgos, "Investigation of hybrid EMI filters for common-mode EMI suppression in a motor drive system," *IEEE Trans. Power Electron.*, vol. 25, no. 4, pp. 1034–1045, Apr. 2010.

[6] X. Wu, D. W. Z. Xu, Y. Okuma, and K. Mino, "Design, modeling, and improvement of integrated EMI filter with flexible multilayer foils," *IEEE Trans. Power Electron*, vol. 26, no. 5, pp. 1344–1354, May 2011.

[7] C. Deng *et al.*, "Integration of both EMI filter and Boost inductor for 1 kW PFC converter," *IEEE Trans. Power Electron.*, vol. 29, no. 11, pp. 5823–5834, Nov. 2014.

[8] R. Chen, J. D. Van Wyk, S. Wang, and W. G. Odendaal, "Improving the characteristics of integrated EMI filters by embedded conductive layers," *IEEE Trans. Power Electron.*, vol. 20, no. 3, pp. 611–619, May 2005.

[9] S. Wang and C. Xu, "Design theory and implementation of a planar EMI filter based on annular integrated inductor–capacitor unit," *IEEE Trans. Power Electron.*, vol. 28, no. 3, pp. 1167–1176, Mar. 2013.

[10] L. Jianjiang, C. Lili, Z. Xuemei, H. Long, L. Cuifen, and C. Lidong, "Design on the planar magnetic integrated EMI filter based on U-shaped magnetic core," in *Proc. 8th Int. Conf. Mech. Intell. Manuf. Technol.*, 2017, pp. 159–163.

[11] J. Biela, A. Wirthmueller, R. Waespe, M. L. Heldwein, K. Raggl, and J. W. Kolar, "Passive and active hybrid integrated EMI filters," *IEEE Trans. Power Electron.*, vol. 24, no. 5, pp. 1340–1349, May 2009.

[12] C. Zhu and T. H. Hubing, "An active cancellation circuit for reducing electrical noise from three-phase AC motor drivers," *IEEE Trans. Electromagn. Compat.*, vol. 56, no. 1, pp. 60–66, Feb. 2014.

[13] K. Lee, D. Xu, B. M. H. Pong, S. Kiratipongvoot, and W. M. Ng, "A three-winding common mode inductor," *IEEE Trans. Power Electron.*, vol. 32, no. 7, pp. 5180–5187, Jul. 2017.

[14] M. L. E. Ali and F. Costa, "Integrated active filter for differential-mode noise suppression," *IEEE Trans. Power Electron.*, vol. 29, no. 3, pp. 1053–1057, Mar. 2014.

[15] S. Jiang, Y. Liu, Z. Mei, X. Pan, J. Peng, and C. Lai, "A magnetic integrated LCL-EMI filter for a single-phase SiC-MOSFET grid-connected inverter," *IEEE J. Emer. Sel. Top. Power Electron.*, vol. 8, no. 1, pp. 601–617, Mar. 2020.

[16] Y. Maillet, R. Lai, S. Wang, F. Wang, R. Burgos, and D. Boroyevich, "High-Density EMI filter design for DC-fed motor drives," *IEEE Trans. Power Electron.*, vol. 25, no. 5, pp. 1163–1172, May 2010.

[17] W. K. Mo and K. M. Paasch, "Hybrid magnetic 3-phase integrated EMI filter," in *Proc. 20th Eur. Conf. Power Electron. Appl.*, 2018, pp. 1–6.

[18] W. Tan, C. Cuellar, X. Margueron, and N. Idir, "A common-mode choke using toroid-EQ mixed structure," *IEEE Trans. Power Electron.*, vol. 28, no. 1, pp. 31–35, Jan. 2013.

[19] Y. Chu, S. Wang, N. Zhang, and D. Fu, "A common mode inductor with external magnetic field immunity, low-magnetic field emission, and high-differential mode inductance," *IEEE Trans. Power Electron.*, vol. 30, no. 12, pp. 6684–6694, Dec. 2015.

[20] N. Zhu, J. Kang, D. Xu, B. Wu, and Y. Xiao, "An integrated AC choke design for common-mode current suppression in neutral-connected power converter systems," *IEEE Trans. Power Electron.*, vol. 27, no. 3, pp. 1228–1236, Mar. 2012.

[21] A. Upadhyay, "Integrated common mode and differential mode inductor device," Patent 5,313,176, May 17, 1994.

[22] H. Zhang, B. Zhang, and S. Wang, "Integrated common mode and differential mode inductors with low near magnetic field emission," in *Proc. IEEE Energy Convers. Congr. Expo.*, 2017, pp. 5375–5382.

[23] Y. Shiraki, S. Yoneda, K. Omae, and T. Nagao, "Inductance analysis for compact dual-mode choke considering magnetic saturation," in *Proc. Int. Symp. Electromagn. Compat.*, 2018, pp. 630–635.

[24] K. Umetani, T. Tera, and K. Shirakawa, "Novel magnetic structure of integrated differential-mode and common-mode inductors to suppress DC saturation," in *Proc. Int. Power Electron. Conf.*, 2014, pp. 304–311.

[25] R. Tallam, G. Skibinski, T. Shudarek, and R. Lukaszewski, "Integrated differential-mode and common-mode filter to mitigate the effects of long motor leads on AC drives," *IEEE Trans. Ind. Appl.*, vol. 47, no. 5, pp. 2075–2083, Sep. /Oct. 2011.

[26] M. Kovacic, Z. Hanic, S. Stipetic, S. Krishnamurthy, and D. Zarko, "Analytical wideband model of a common-mode choke," *IEEE Trans. Power Electron.*, vol. 27, no. 7, pp. 3173–3185, Jul. 2012.

[27] P. C. Krause, O. Wasynczuk, and S. D. Sudhoff, *Analysis of Electric Machinery and Drive Systems*. Piscataway, NJ, USA: IEEE Press, 2002.

[28] M. L. Heldwein, L. Dalessandro, and J. W. Kolar, "The three-phase common-mode inductor: Modeling and design issues," *IEEE Trans. Ind. Electron.*, vol. 58, no. 8, pp. 3264–3274, Aug. 2011.

[29] M. J. Nave, "On modeling the common mode inductor," in *Proc. IEEE Int. Symp. Electromagn. Compat.*, 1991, pp. 452–457.

[30] H. Chen, Z. Qian, S. Yang, and C. Wolf, "Finite-element modeling of saturation effect excited by differential-mode current in a common-mode choke," *IEEE Trans. Power Electron.*, vol. 24, no. 3, pp. 873–877, Mar. 2009.

[31] M. Pozar, *Microwave Engineering*. Hoboken, NJ, USA: Wiley, 2012.

[32] K. Tsai, "EMI modeling and characterization for ultra-fast switching power circuit based on SiC and GaN Devices," Ph.D. dissertation, Dept. Elect. and Comput. Eng., Ohio State Univ., Columbus, OH, USA, 2013.

[33] R. Lai, Y. Maillet, F. Wang, S. Wang, R. Burgos, and D. Boroyevich, "An integrated EMI choke for differential-mode and common-mode noise suppression," *IEEE Trans. Power Electron.*, vol. 25, no. 3, pp. 539–544, Mar. 2010.

[34] K. Kostov and J. J. Kyyrä, "Insertion loss and network parameters in the analysis of power filters," in *Proc. Nordic Workshop Power Ind. Electron.*, Finland, Jun. 9–11, 2008.

[35] S. Wang, F. C. Lee, and W. G. Odendaal, "Characterization, evaluation, and design of noise Separator for conducted EMI noise diagnosis," *IEEE Tran. Power Electron.*, vol. 20, no. 4, pp. 974–982, Jul. 2005.

Javad Borsalani was born in Iran in 1988. He received the B.S. and M.S. degrees in electrical engineering from the Shahrood University of Technology, Shahrood, Iran, in 2010 and 2012, respectively. He is currently working toward the Ph.D. degree with the Faculty of Electrical and Robotic Engineering, Shahrood University of Technology, Shahrood, Iran.

His main research interests include electromagnetic compatibility of power electronics and the design and development of new-type EMI filters.

Ali Dastfan was born in Iran, in 1966. He received the B.E. degree from the University of Ferdowsi, Mashhad, Iran, in 1989, and the M.E. and Ph.D. degrees from the University of Wollongong, Wollongong, NSW, Australia, in 1994 and 1998, respectively, all in electrical engineering.

He is currently with the Faculty of Electrical and Robotic Engineering, Shahrood University of Technology, Shahrood, Iran. His research interests include power electronics and power quality.

Javad Ghalibafan received the B.S. degree from the Ferdowsi University of Mashhad, Mashhad, Iran, in 2007, and the M.S. and Ph.D. degrees from the Iran University of Science Technology, Tehran, Iran, in 2009 and 2013, respectively.

In 2014, he joined the Faculty of Electrical and Robotic Engineering, Shahrood University of Technology, Shahrood, Iran, where he is currently an Associate Professor, and the Head of Antenna & Microwave Lab. His research interests include the analysis, design, and measurement of artificial electromagnetic materials; antenna and microwave devices; metamaterial; and magnetic material.